

# Accounts of Materials & Surface Research

## Highly Nanoporous Graphene Monoliths

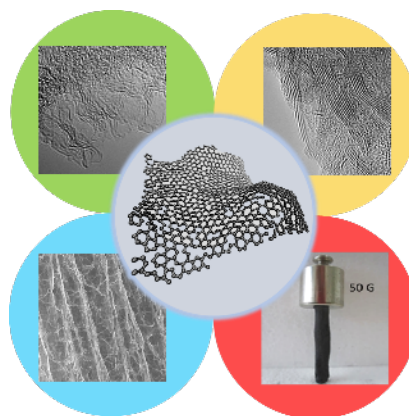
Shuwen Wang\* and Katsumi Kaneko

Center for Energy and Environmental Science, Shinshu University  
s\_wang@shinshu-u.ac.jp

### Abstract

The porosity control of graphene-based carbons is introduced in this paper. A series of methods like chemical reagent activation, CO<sub>2</sub> activation and thermal treatment are examined in detail. KOH activation can produce graphene-based carbons with higher surface area and wider porosity tunability than CO<sub>2</sub> activation or chemical reagent activation with ZnCl<sub>2</sub> or H<sub>3</sub>PO<sub>4</sub>. Thermal treatment of highly porous graphene monolith in temperature range of 1073 K to 3073 K results in a wide surface area distribution from 1560 m<sup>2</sup>g<sup>-1</sup> to 10 m<sup>2</sup>g<sup>-1</sup> according to the subtracting pore effect (SPE) method. The study from transmission electron microscopic (TEM), X-ray diffraction (XRD) and Raman spectroscopy illustrate the evolution of microscopic morphology and crystallinity of the porous graphene monolith.

Besides, a shape-retention activation method is introduced for preparing highly microporous graphene monolith of free-standing geometry and well-aligned textures, and a polymer enhancing method is provided for preparing highly sturdy monolith through the soaking the RGO monoliths with a poly(ammonium-4-styrene sulfonate) followed by heat treatment.



**Keyword:** Nanopore, Graphene, Carbon activation, Adsorption, Graphene oxide

Shuwen Wang received his PhD (2012) in chemistry from the Chiba University (Japan). During his PhD he conducted research on the CO<sub>x</sub>-free hydrogen production from CH<sub>4</sub> decomposition. He joined Prof. K. Kaneko's group in Research Center for Exotic Nanocarbons in Shinshu University (Japan) since 2012 and worked on highly-porous graphene-based materials. He then moved to the group of Prof. D.Y. Zhao in Fudan University (China) in 2015 and worked on hierarchical nanostructures. Since July 2017 he moved back to Shinshu University (Japan) to work with Prof. K. Kaneko. His current research focuses on the investigation of 2-dimensional confined nanopores for applications in catalysis and energy converting.



Katsumi Kaneko is distinguished professor Shinshu University since April, 2010. He moved from Graduate School of Science, Chiba University to Shinshu University in 2010. He graduated the master program of Chemistry of The University of Tokyo in 1971. Doctor of Science was awarded to research achievement in Chiba University by The University of Tokyo in 1977. He has developed nanospace molecular science, challenging to nanospaces nanomaterials engineering. He published more than 470 papers on international journals. His achievements were awarded by Chemical Society of Japan in 1999, by American Carbon Society in 2007, and by American Institute of Chemical Engineering in 2016. He was in charge of president of International Adsorption Society from 2004 to 2007. He is fellow of Royal Society of Chemistry, International Adsorption Society, and Chemical Society of Japan.



# Highly nanoporous graphene monoliths

## 高度のナノ細孔を有するグラフェンモノリス

Shuwen Wang\* and Katsumi Kaneko

Center for Energy and Environmental Science, Shinshu University

### 1. Introduction

Promotion of renewable energy has been intensively demanded to improve our earth environment. The renewable energy is intermittent and highly region-dependent. We must develop efficient energy storage method, energy saving method and interregional exchange system for stationary supply of the renewable energy.

Nanoporous carbons of high electrical conductivity are indispensable to innovate efficient storage and saving methods of energy<sup>1-3</sup>). Nanoporous carbon has been widely applied to supercapacitors<sup>4-6</sup>), being one of the representative energy storage. Renewable energy-derived fuel production and electrochemistry for CO<sub>2</sub> reduction are also strongly associated with porous carbons. Thus the role of nanoporous carbons becomes increasingly important. However, the main nanoporous carbon is activated carbon whose structure is not fully understood. Therefore, we must challenge to innovate nanoporous carbons whose characteristics is highly improved. One promising route is a bottom up method using nanoscale graphene units derived from graphene oxide colloids<sup>7-9</sup>).

This review describes how to prepare

highly nanoporous graphene of better electrical conductivity. As chemistry of nanoporous carbon depends on the morphology, we focus on the nanoporous graphene monolith which has great advantages on application. The monolithic structure with 3-dimensional networks provides fast mass diffusion and good electronic transportation. Furthermore, the designable shape and mechanical stability of a monolith are also important for industrial applications. However, development of highly nanoporous graphene monoliths could not be easily carried out. This article introduces the step-by-step processes to succeed to obtain the highly nanoporous graphene monoliths<sup>9-12</sup>).

### 2. KOH activation

KOH activation method is one of the most effective way to develop the porosity on carbon materials. This activation process consists of several redox reactions in which carbon is oxidized to carbonate and CO<sub>x</sub>, while KOH is converted into K<sub>2</sub>CO<sub>3</sub> or reduced into metallic potassium<sup>13, 14</sup>). The breaking down and separation of graphitic structure in the carbon leads to the formation of nanoporosity.

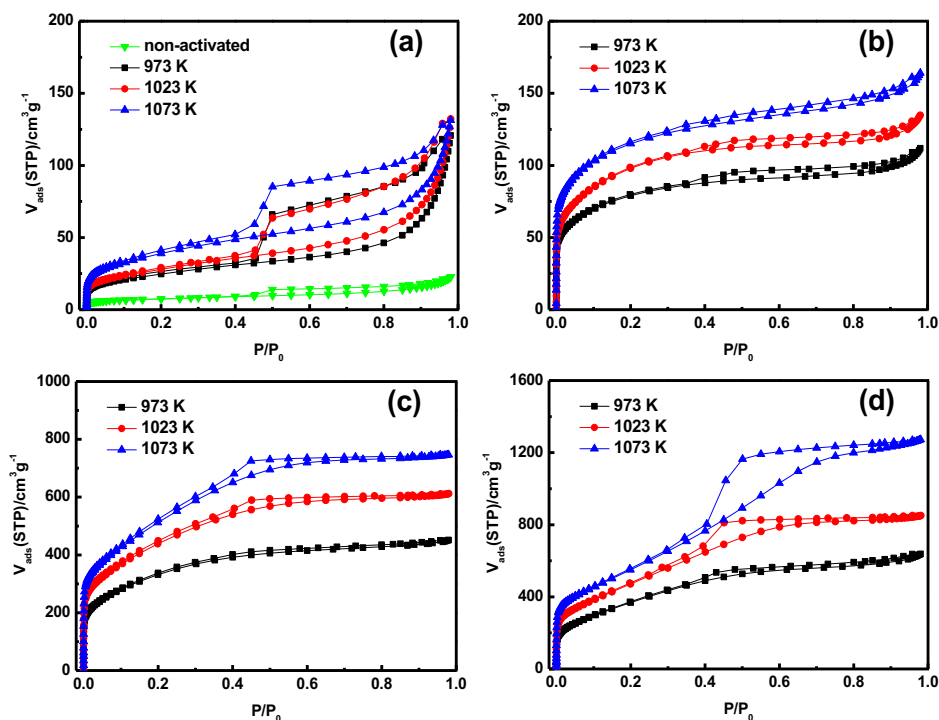


**Figure 1.**  $N_2$  adsorption-desorption isotherms (77.4 K) of porous graphene monolith prepared by KOH activation at different temperatures with  $KOH/C = 1$  (a), 2 (b), 3 (c) and 5 (d). Reproduced with permission from Ref. 9.

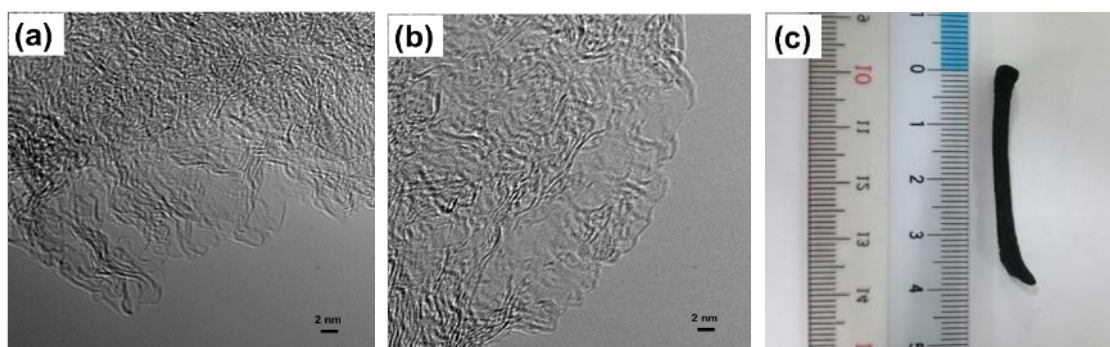


**Figure 2.** High-resolution TEM (HR-TEM) images and a photo of PGM prepared from KOH activation at 1073 K with  $KOH/C = 5$ . Reproduced with permission from Ref. 9.

The graphene oxide (GO) colloid was firstly prepared by a modified Hummer method<sup>15</sup>. The GO monoliths were produced from unidirectional freeze drying method introduced by the previous works<sup>16, 17</sup>. The reduced GO (RGO) monoliths can be obtained through the heat treatment of GO monoliths in Ar atmosphere. The preparation of porous graphene monolith (PGM) with KOH activation was carried out

by a one-step activation method, i.e., before the activation process, KOH were mixed with GO suspensions at different KOH to carbon weight ratio ( $KOH/C$ ) in advance, then the PGM were produced from the mixtures using the unidirectional freeze drying followed by reduction and activation at certain temperatures.

Figure 1(a) shows the  $N_2$  adsorption-desorption isotherms of RGO monolith and

**Table 1.** Porosity parameters for RGO and PGM prepared under varying conditions. Reproduced with permission from Ref. 9.

Activation conditions	$S_{as}$ ( $m^2 g^{-1}$ )	$S_{BET}$ ( $m^2 g^{-1}$ )	$S_{as-external}$ ( $m^2 g^{-1}$ )	$V_{DR}$ ( $cm^3 g^{-1}$ )
None	24	26	--	--
KOH/C = 1, 973 K	78	87	54	0.02
1023 K	90	100	68	0.03
1073 K	123	123	86	0.05
KOH/C = 2, 973 K	270	270	28	0.10
1023 K	320	335	20	0.11
1073 K	405	415	65	0.14
KOH/C = 3, 973 K	1060	1100	80	0.39
1023 K	1400	1450	58	0.53
1073 K	1645	1765	50	0.61
KOH/C = 5, 973 K	1080	1160	185	0.42
1023 K	1450	1510	100	0.59
1073 K	1760	1840	325	0.67
KOH/C = 10, 1073 K	2150	2200	360	0.81

PGMs prepared with KOH/C = 1 at different temperatures. Both the RGO and PGMs have the adsorption isotherms of type IV with a slight combination of type I, indicating the predominant mesoporosity with a little microporosity. Comparing with the RGO, the adsorption isotherms from PGMs show an evident enhancement of  $N_2$  uptake in whole  $P/P_0$  region, suggesting the remarkable porosity development. The  $N_2$  adsorption-desorption isotherms of PGMs prepared with KOH/C = 2 are shown in Figure 1(b). These isotherms show much less characteristic of type IV but more characteristic of type I comparing with those prepared with KOH/C = 1, indicating the deterioration of mesoporous structure accompanied by the development of micropores. A slight adsorption uptake can be

observed at  $P/P_0$  close to 1 in each adsorption isotherms, suggesting that wide mesopores and macropores still remain after the activation process. The samples prepared with KOH/C = 3 show a significant enhancement of  $N_2$  uptake at  $P/P_0 < 0.4$ , as shown in Figure 1(c), which comes from the highly developed micropores, especially the large micropores<sup>18)</sup>. The adsorption isotherms are almost saturated at  $P/P_0 > 0.5$ , being indicative of disappearance of wide mesopores and macropores. The notable hysteresis shown at  $P/P_0 = 0.4 \sim 0.6$  for samples prepared at 1023 K and 1073 K suggest the presence of small mesopores, which is derived from the continuously enlargement of micropores by degradation and burning of graphene units. For PGMs prepared with

KOH/C = 5, an even larger initial  $N_2$  uptake amount in the low  $P/P_0$  region can be observed, as shown in Figure 1(d), suggesting the further development of microporosity. Besides, isotherms of PGMs obtained at 1023 K and 1073 K show a gradual  $N_2$  uptake increase at  $P/P_0 > 0.4$  with distinct hysteresis loop, suggesting the presence of newly developed mesoporosity from the ever enlarging microporosity. Their hysteresis with a horizontal desorption branch at high  $P/P_0$  region together with a steep drop are classified as Type H2 according to IUPAC classification<sup>19</sup>. In the past the Type H2 hysteresis was attributed to 'ink bottle' pore effect due to the difference in condensation and evaporation in pores with narrow necks and wide bodies, but now it is considered this model is over-simplified because the role of network effects should be taken into account. The porosity parameters determined from above adsorption-desorption isotherms are given in Table 1.

The microscopic structure and a photo of

2. The entangled and crumpled graphene sheets construct the three dimensional (3D) network with abundant nanospaces, i.e., the meso- and microporosity as previously mentioned. Different from conventional high surface area activated carbons (or activated carbon fibers) that mainly consist of graphene unit of a few nanometers in scale<sup>20, 21, 22</sup>, the graphene monolith is constructed by graphene sheets with considerably integrated structure and large size, being responsible for its enhanced mechanical stability. The graphene monoliths in this study still maintain their free-standing nature after the activation at 1073 K. However, a shape deformation is observed on the graphene monolith, this is caused by the shrinkage of monolith occurs during the freeze drying step. Consequently, it is necessary to develop new methods for preparing graphene monolith without structural deformation. In the following chapters a modified KOH activation route for producing graphene monoliths with better structural designability will be introduced.

Based on the porosity parameters and

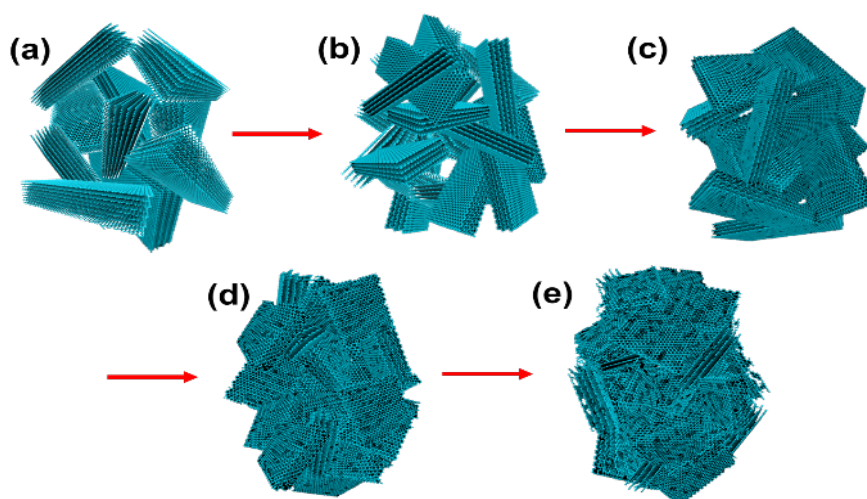


**Figure 3.** Model of porosity development on PGM. (a) un-activated RGO; PGM activated at 1073 K with (b) KOH/C = 1, (c) KOH/C = 2, (d) KOH/C = 3 and (e) KOH/C = 5.

the graphene monoliths from RGO activated at 1073 K with KOH/C = 5 is shown in Figure

TEM observation, a simple activation model can be proposed for describing the

porosity development on PGMs with the KOH/C ratio increase from 1 to 5, as shown in Figure 3. The pristine RGO without KOH activation contains stacked graphene layers which are randomly bridging with each other, as shown in Figure 3(a). The interspaces constructed by those stacked graphene layers are macropores in general. KOH activation with KOH/C = 1 can break up the stacked graphene layers into thinner and finer pieces, bringing the smaller interspaces, as shown in Figure 3(b). KOH activation with KOH/C = 2 leads to the formation of more defective graphene layers and correspondingly, the formation of micropores, as shown in Figure 3(c). However, some mesoporous spaces still remain under this activation condition. These remained mesoporous space is filled with newly produced single and/or few layers of graphene by increasing the KOH/C ratio to 3, as shown in Figure 3(d). Activation with KOH/C = 5 exfoliates more few-layered graphene into single layers.

Meanwhile, intensive gasification brings about the increase of pore size and the formation of mesopores (Figure 3(e)). It is possible to obtain the target porosity of graphene-based porous carbon by using this activation model. However, this model should not be applied to conventional activated carbons which have no well-defined structures.

### 3. CO<sub>2</sub> activation

CO<sub>2</sub> activation of carbon materials is based on the gasification reaction between CO<sub>2</sub> and carbon atoms of carbon precursor. The porosity can be developed through the extraction of carbon atoms from the carbon structure. The CO<sub>2</sub> activation method introduced in this review was conducted by feeding 30% CO<sub>2</sub> in Ar at a flow rate of 200 mL min<sup>-1</sup> with varying activation time and temperature. The pristine RGO monolith was used as carbon precursor for CO<sub>2</sub> activation.

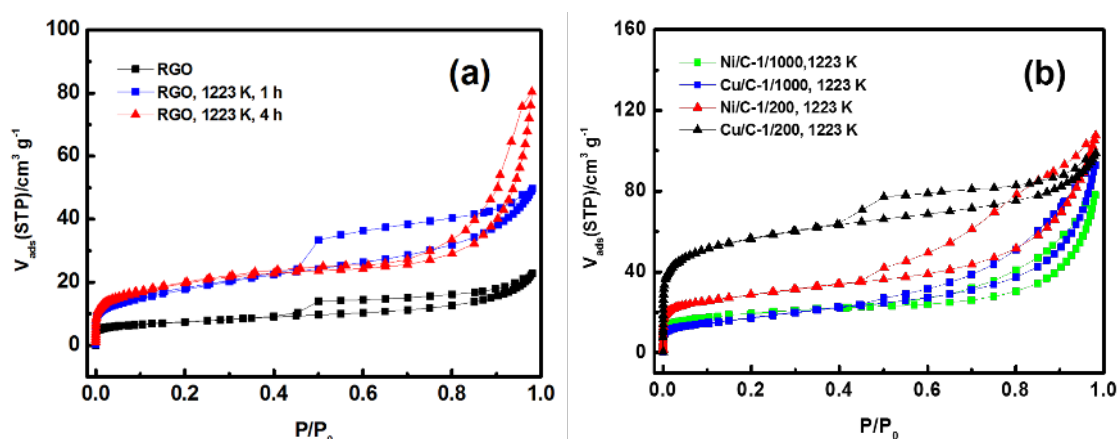


**Figure 4.** N<sub>2</sub> adsorption-desorption isotherms (77.4 K) of (a) RGO activated by CO<sub>2</sub> at 1223 K for 1 h and 4h, and (b) metal loaded RGO activated by CO<sub>2</sub> at 1223 K for 2 h. Reproduced with permission from Ref. 9.

**Table 2.** Porosity parameters of RGO and metal loaded RGO after CO<sub>2</sub> activation at 1223 K.

Sample	S <sub>BET</sub> (m <sup>2</sup> /g)	S <sub>as</sub> (m <sup>2</sup> /g)	S <sub>as-external</sub> (m <sup>2</sup> /g)	V <sub>DR</sub> (cm <sup>3</sup> /g)	Burn off (wt%, ± 5%)
H-RGO	26	24	--	--	--
H-RGO, 1 h	63	57	41	0.02	21
H-RGO, 4 h	70	64	18	0.03	79
Ni/C-1/1000, 2h	67	72	20	0.03	48
Cu/C-1/1000, 2h	62	58	48	0.02	46
Ni/C-1/200, 2h	100	105	50	0.04	71
Cu/C-1/200, 2h	205	205	52	0.08	64

The N<sub>2</sub> adsorption-desorption isotherms of RGO monoliths activated at 1223 K for 1 h and 4h are shown in Figure 4(a). The isotherms of activated RGO monoliths are both of type IV but the hysteresis loop changes from H4 to H3<sup>19)</sup> with the increase of activation time. The adsorption isotherm of sample produced from 4 h of activation gives a steeper uptake at higher P/P<sub>0</sub> region, indicating the broadening of mesopores after longer time of activation. The surface areas for the samples activated for 1 and 4 h are 57 and 64 m<sup>2</sup> g<sup>-1</sup> according to the SPE method, respectively. Marsh<sup>23)</sup> reported that a trace amount of metal in carbon can play a significant role in the gasification reaction. The RGO monoliths prepared in this work experienced several times of acid washing during the preparation process, then the metal content in carbon should be very low. We examined the CO<sub>2</sub> activation on RGO monoliths loaded with Ni or Cu at metal to carbon mole ratio of 1/1000 and 1/200, as shown in Figure 4(b) and Table 2. Comparing with CO<sub>2</sub> activation over other carbon materials<sup>24, 25)</sup>, the porosity of RGO

monoliths are still small by all means we have tried. This should be ascribed to that on the basal planes the CO<sub>2</sub> molecules undergo a reaction only at a speed of 10<sup>-2</sup> to 10<sup>-3</sup> order of that at the edges of the graphene planes (prismatic edges)<sup>26)</sup>. The RGO monoliths developed in this work has more basal planes but less prismatic edges comparing with conventional carbons, then the CO<sub>2</sub> activation method is not effective for the porosity development.

#### 4. ZnCl<sub>2</sub> and H<sub>3</sub>PO<sub>4</sub> activation

ZnCl<sub>2</sub> and H<sub>3</sub>PO<sub>4</sub> can be used for activating carbon materials based on their dehydrating effect. Similar to the KOH activation method as already introduced, the GO monoliths with chemical reagent was prepared through unidirectional freeze drying method in advance for further activation. The carbon to chemical reagents weight ratio was prepared as 1 to 1. The ZnCl<sub>2</sub>-contained monoliths were activated at the temperature of 773 K and 873 K, while H<sub>3</sub>PO<sub>4</sub>-contained RGO monoliths were activated at the temperature of 623 K and 673 K. The activation conditions used

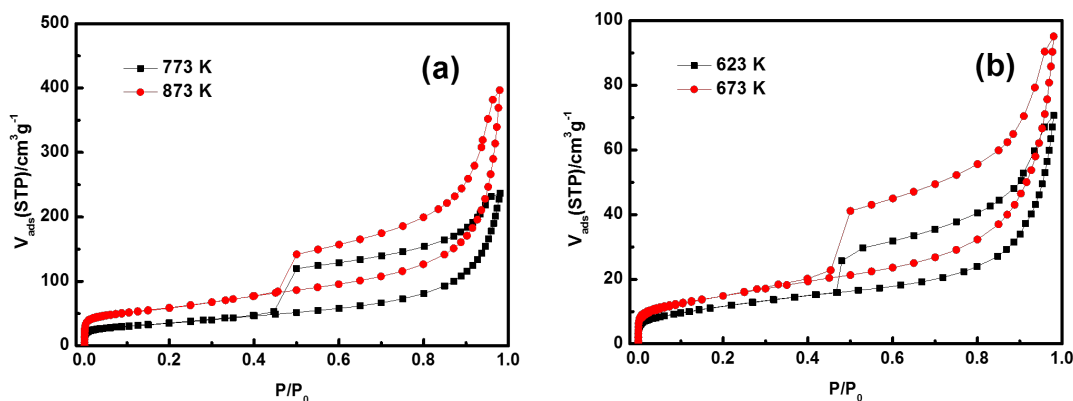


**Figure 5.** N<sub>2</sub> adsorption-desorption isotherms (77.4 K) of RGO activated by (a) ZnCl<sub>2</sub> and (b) H<sub>3</sub>PO<sub>4</sub>. Reproduced with permission from Ref. 9.

here are according to the reported optimized conditions<sup>27-30</sup>.

N<sub>2</sub> adsorption-desorption isotherms of RGO monoliths activated by ZnCl<sub>2</sub> at 773 K and 873 K are shown in Figure 5(a). The isotherms are of typical type IV according to the IUPAC classification. A distinct hysteresis with a steep uptake at high P/P<sub>0</sub> region can be observed, indicating the presence of wide mesopores. The surface areas evaluated by SPE method are 210 and 120 m<sup>2</sup> g<sup>-1</sup>, respectively, as shown in Table 3. The relatively small surface area and typical type IV isotherms indicates the insufficient development of micropore. RGO monoliths activated by H<sub>3</sub>PO<sub>4</sub> show similar adsorption isotherm to those of

ZnCl<sub>2</sub>-activation in shape with less adsorption amount, as shown in Figure 5(b), indicating that activation with H<sub>3</sub>PO<sub>4</sub> also mainly produce wide mesopores and external surfaces but at a less developed level comparing with ZnCl<sub>2</sub>. The porosity parameters shown in Table 3 suggests that the surface area and micropore volume of the samples developed in this work are much lower than those in the previously reported works<sup>27-30</sup>.

The effect of porosity development on carbon material through ZnCl<sub>2</sub> or H<sub>3</sub>PO<sub>4</sub> activation should largely depends on the property of the precursor used. Activation of vegetal precursor with ZnCl<sub>2</sub> or H<sub>3</sub>PO<sub>4</sub> at high temperature leads to the dehydration

**Table 3.** Porosity parameters for RGO activated by ZnCl<sub>2</sub> and H<sub>3</sub>PO<sub>4</sub>. Reproduced with permission from Ref. 9.

Sample	S <sub>BET</sub> (m <sup>2</sup> /g)	S <sub>as</sub> (m <sup>2</sup> /g)	S <sub>as-external</sub> (m <sup>2</sup> /g)	V <sub>DR-micro</sub> (cm <sup>3</sup> /g)
H-RGO	26	24	--	--
ZnCl <sub>2</sub> , 773 K, 1h	125	120	105	0.04
ZnCl <sub>2</sub> , 873 K, 1h	210	210	170	0.08
H <sub>3</sub> PO <sub>4</sub> , 623 K, 1h	40	36	33	0.01
H <sub>3</sub> PO <sub>4</sub> , 673 K, 1h	53	49	43	0.02

of the cellulose, hemicellulose and lignin compounds in precursor, leaving porosity in the carbon matrix<sup>26)</sup>. On the other hand, GO based carbon materials do not exhibit such dehydrating effect due to their much ordered structure and less aquo-complex, giving less developed porosity structure comparing with the plants-originated activated carbons. Even so, RGO monolith produced from ZnCl<sub>2</sub>-activation contains considerable amount of mesoporosity, being a potential material for catalyst supports or adsorbents for biomacromolecule.

## 5. Thermal treatment

Heat treatment of carbon materials at high temperature is a commonly used method for improving their crystallinity and reducing the defects<sup>31, 32)</sup>, although a significant decrease of porosity can happen due to the stacking of graphitic units<sup>33, 34)</sup>. In the present review, we will introduce the heat treatment of PGM up to 3073 K with a

atmosphere. The porous graphene monolith treated at temperature of  $T$  is nominated as PGM- $T$ . The PGM is prepared by the same route as mentioned in previous chapter but from a different batch. The porosity of PGM can be effectively tuned through the thermal treatment. Furthermore, part of the excellent properties of well-defined graphitic structure can be recovered, which is highly required for the applications need both high surface area and good electrical conductivity.

N<sub>2</sub> adsorption-desorption isotherms (77.4 K) for pristine and heat treated PGM are shown in Figure 6(a). Heat treatment at temperatures below 1373 K doesn't give significant porosity change of PGM according to the N<sub>2</sub> adsorption-desorption isotherms. At heating temperature above 1373 K, the N<sub>2</sub> uptake amount in the low  $P/P_0$  region of isotherms starts to decrease with the increase of temperature, indicating the degradation of micropores. The iso-

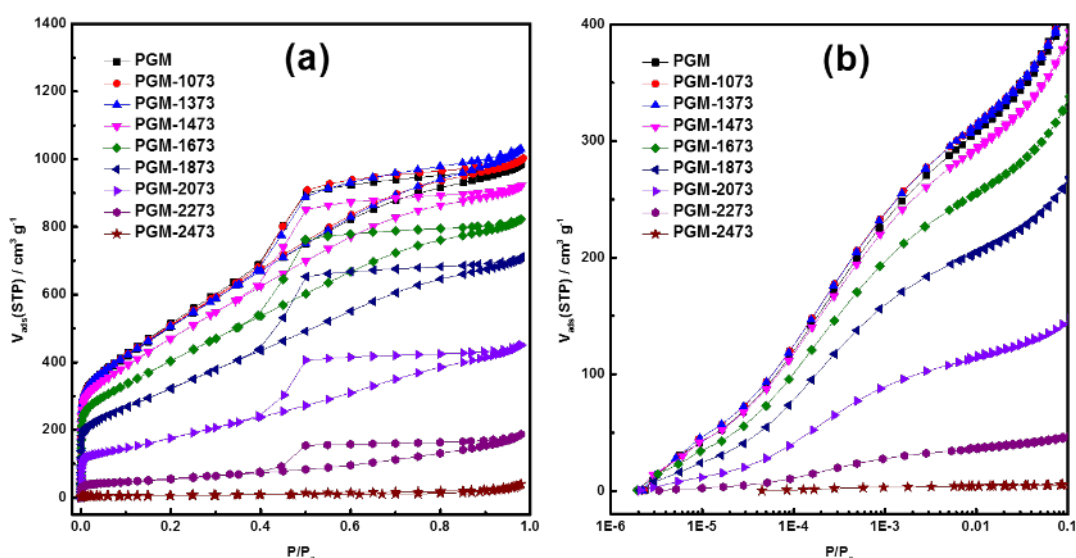


**Figure 6.** (a) N<sub>2</sub> adsorption-desorption isotherms (77.4 K) and (b) their corresponding logarithmic curves at  $P/P_0 < 0.1$  for PGM and PGM-T samples. Reproduced with permission from Ref. 10.

graphite-resistance furnace under the Ar

therm of PGM-1473 shows a slower up-

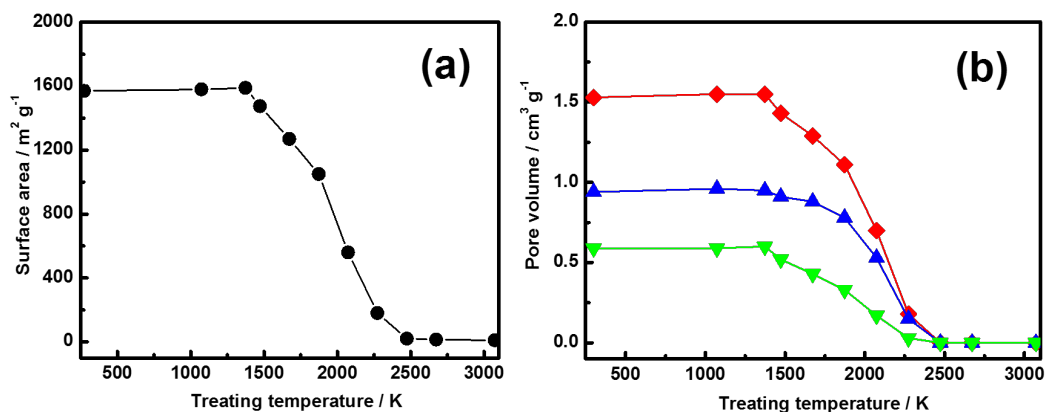


**Figure 7.** (a) Surface area and (b) Pore volume evolution of PGM during heat treatment. Surface area: ●, total pore volume: ◆, mesopore volume: ▲, micropore volume: ▼. Reproduced with permission from Ref. 10.

ward structure on desorption branch comparing with the samples treated at lower temperatures, suggesting its characteristic of H4 become weaker and that of type H2 becomes more distinct. The hysteresis loops become typical type H2 for samples treated at temperature above 1473 K, as shown in the isotherms of PGM-1673, PGM-1873 and PGM-2073. For samples treated at an even higher temperature of

2273 K and 2473 K, the hysteresis loop becomes less evident and finally disappears. The detailed  $N_2$  adsorption isotherms in the submonolayer region are shown in Figure 6(b).

The change of the surface area and pore volume of samples with heating temperature are shown in Figure 7. The surface area shows no significant change with heating temperature up to 1373 K, then

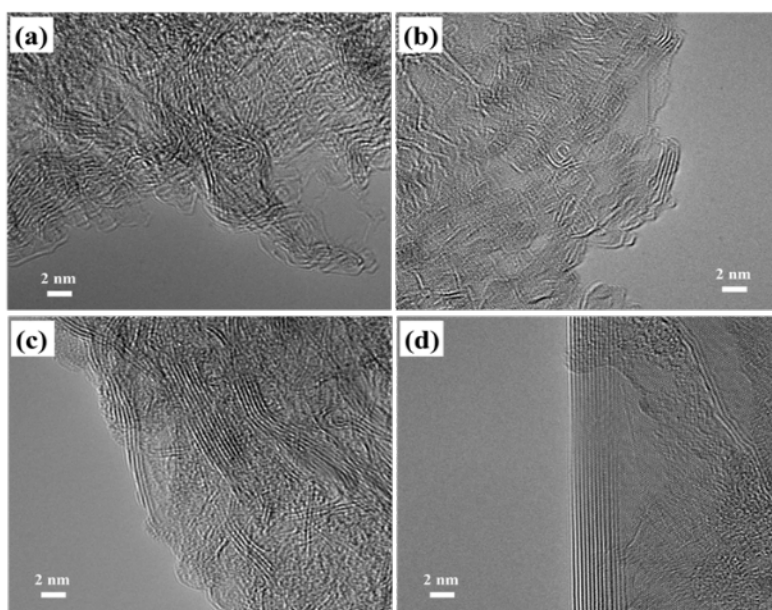


**Figure 8.** HR-TEM images of (a) PGM, (b) PGM-1873, (c) PGM-2273, and (d) PGM-2673. Reproduced with permission from Ref. 10.

decreases with elevation of the temperature. Heat treatment at the high temperature of 2473 K gives only  $20 \text{ m}^2 \text{ g}^{-1}$  of surface area. The change of pore volume with the heating temperature is similar to that of the surface area, experiences a stable state with heating temperature up to 1373 K and a remarkable decrease at higher temperatures. It is noticed that all of the total pore volume, mesopore volume and micropore volume decrease in a similar way with the heating temperature. Consequently, the stacking of graphene layers should occur uniformly within all the nanoporous structure.

The morphology change of graphene sheets during the heat treatment is observed by a high-resolution TEM, as shown in Figure 8. The non-treated PGM mainly consists of monolayer or few layer graphene sheets entangling with each other, as shown in Figure 8(a). After heat treatment at 1873 K, the distorted graphene

kled surface, as shown in Figure 8(b), which is a transitional state between highly entangled graphene networks and ordered graphitic structures. After heat treatment at 2273 K, the stacking graphene with large-scale of uniformity and well-aligned graphene sheets are formed, as shown in Figure 8(c), indicating the disordered stacking graphene start to reconstruct itself into graphitic structure. The well-crystalline graphitic layer structure can form at an even high treating temperature of 2673 K, as shown in Figure 8(d). However, the disordered graphitic parts still coexist with the ordered graphitic parts, i.e., the growth of graphitic layers should only consume the crystallizable part, leaving the disordered structures.

Raman spectra of PGM-T samples are shown in Figure 9 (a). Two overlapping broad bands locating at  $\sim 1350 \text{ cm}^{-1}$  (D band) and  $\sim 1590 \text{ cm}^{-1}$  (G band) correspond to the defective part of carbon and

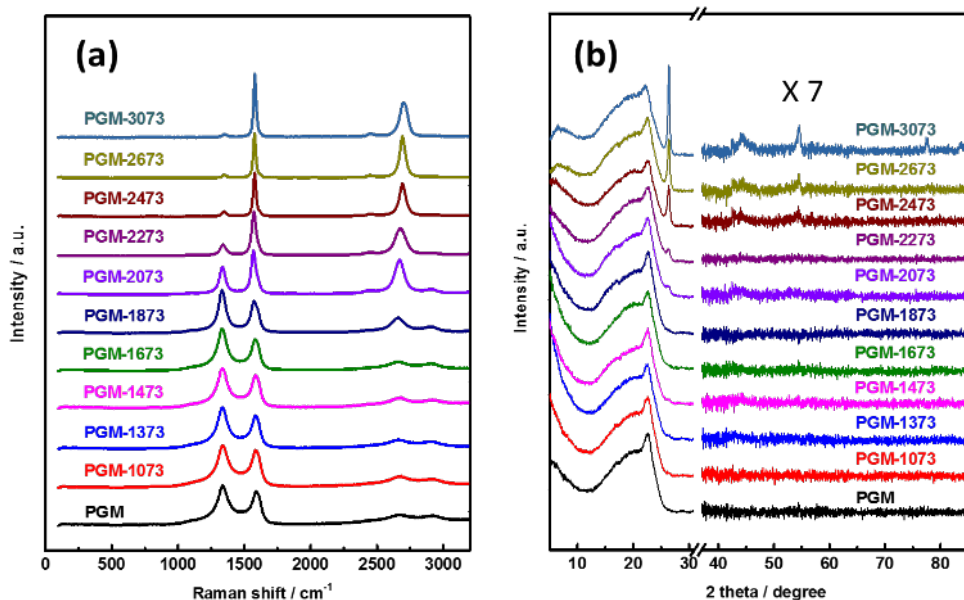


**Figure 9.** Raman spectra and X-ray diffraction patterns of PGM and PGM-T samples. Reproduced with permission from Ref. 10.

sheets convert into small bricks with wrin-

the stretching vibration in the aromatic

planes, respectively. No significant variation of Raman spectra is observed on both bands at the heating temperature below 1873 K, while at the treating temperature above 1873 K the decrease of D band and increase and sharpening of the G band start to occur. The  $I_D/I_G$  ratio decreases continuously from 1.52 to 0.11, indicating an effective graphitization process of PGM through heat treatment. Meanwhile, the peak at  $2450\text{ cm}^{-1}$  corresponding to the overtone mode longitudinal optical phonons<sup>35)</sup> starts to appear, the 2D band (also called G' band) locating at  $2700\text{ cm}^{-1}$ <sup>36)</sup> becomes distinct and sharp, and the peak locating at  $2930\text{ cm}^{-1}$  known as (D + G) combination mode<sup>37)</sup> becomes weaker and

finally diminishes with the increasing temperature. All these results suggest the local reconstruction of disordered and defective graphene layers into ordered graphitic structure during the thermal treatment. The in-plane size of graphitic crystallites ( $L_a$ ) can be obtained by using the Tuinstra-Koenig equation<sup>38,39)</sup>:

$$I_D / I_G = C(\lambda) / L_a$$

Here the C (514.5 nm) value is  $\sim 4.4\text{ nm}$  according to reference<sup>40)</sup>. The obtained  $L_a$  value are shown in Table 4.

X-ray diffraction patterns of PGM and PGM-T samples are shown in Figure 9(b). For non-heated PGM there is only a broad peak at  $22.6^\circ$  can be observed, indicating the non-crystalline structure. Heat treatment at temperature below 1873 K

**Table 4.** Parameters obtained from X-ray diffraction patterns and Raman spectra. Reproduced with permission from Ref. 10.

Sample	XRD			Raman	
	$d_{002}$ (nm)	$L_c$ (nm)	$N_c$	$I_D / I_G$	$L_a$ (nm)
PGM	--	--	--	1.82	2.4
PGM-1073	--	--	--	1.79	2.5
PGM-1373	--	--	--	1.87	2.4
PGM-1473	--	--	--	1.79	2.5
PGM-1673	--	--	--	1.75	2.5
PGM-1873	--	--	--	1.52	2.7
PGM-2073	0.338	3.8	11.2	0.83	5.3
PGM-2273	0.338	5.9	17.5	0.38	11.6
PGM-2473	0.337	12.7	37.5	0.19	23.2
PGM-2673	0.337	17.5	51.9	0.14	31.4
PGM-3073	0.337	22.1	65.6	0.11	40.0

doesn't give significant change of the X-ray diffraction patterns, suggesting the high energy barrier for the mutual ordering of graphene layers. At heating temperature above 1873 K the (002) peak of graphite starts to appear at  $26.4^\circ$  and becomes sharper, indicating the growth of well-ordered graphitic structure. For samples heated at even higher temperatures above 2473 K, the peak (100) and (101) at around  $44^\circ$ , peak (004) at around  $55^\circ$ , peak (110) at around  $78^\circ$  and peak (112) at around  $83.5^\circ$  start to appear, suggesting the formation of higher level of crystallinity and partially recovery of the graphitic structure 41).

The mean size of the graphitic crystal along the c axis ( $L_c$ ) can be determined by the Scherrer's equation with the half width

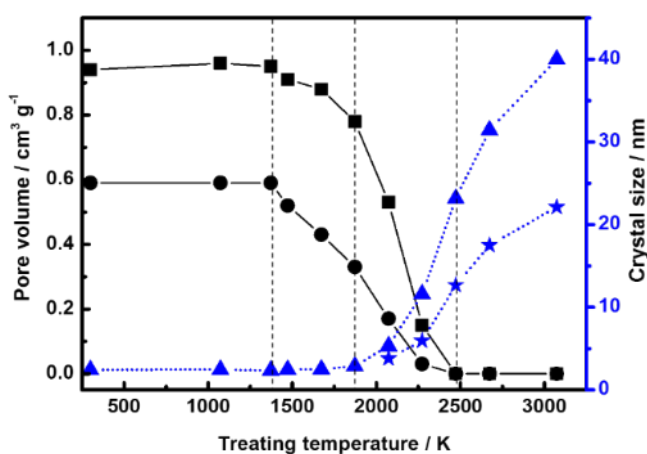


**Figure 10.** Comparison between the crystallite size parameters and pore volume at different heating temperatures. Mesopore volume: ■, micropore volume: ●, in-plane size of graphite crystallites  $L_a$ : ▲, mean crystallite size along the c axis  $L_c$ : ★. Reproduced with permission from Ref. 10.

of the sharp (002) peaks 42) and the average graphene layer number  $N_c$  can be determined by means of the simple equa-

tion  $N_c = L_c / d_{002}$ . The obtained results are shown in Table 4.

In order to get a better understanding of the structural evolution with heating temperature, the changes of micropore volume, mesopore volume and the crystallite size parameters like  $L_c$  and  $L_a$  are plotted together in Figure 10 for comparison. The structural evolution of PGM can be divided into 4 distinct stages which happen within the temperature regions of (A):  $T < 1373$  K, (B):  $1373$  K  $< T < 1873$  K, (C):  $1873$  K  $< T < 2473$  K, and (D):  $T > 2473$  K, respectively. No obvious change occurs in temperature region (A). In region (B) the crystalline state of PGM do not change but the porosity starts to decrease, indicating the energy barrier for the stacking of graphene layers is lower than formation of graphitic crystallite. This is because the growth of graphitic crystallite requires both coalescence of the edge bonding and in-plane arrangement of graphene layers 43, 44), whereas the partial stacking of graphene crystallites can be achieved by slight translational motion of the graphene layers. Thermal treating at temperature region (C) enables coalescence of the mutual edges of the graphene layers to give the in-plane graphene growth as well as the stacking of the well-developed graphene sheets, resulting in an even decreased porosity. Further stacking and coalescence of graphene crystallites occurs in the temperature region (D), diminishing almost all the porosity and bringing well-crystalline graphitic structure. However, even the samples treated at 3073 K have the mixed structure of both well-crystalline graphite and the disordered graphitic parts according to the

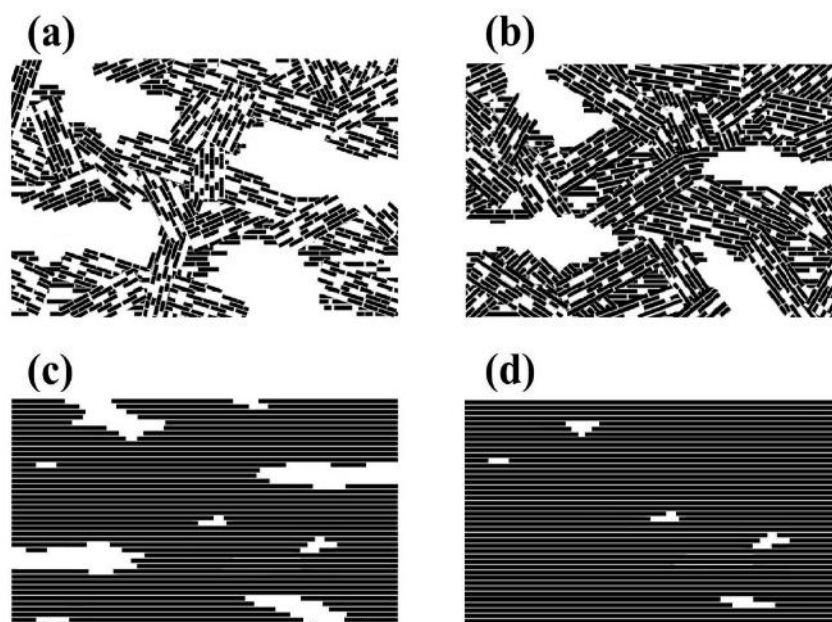


**Figure 11.** Structural evolution model of PGM thermal treated at different temperature regions. (a)  $T < 1373$  K, (b)  $1373$  K  $< T < 1873$  K, (c)  $1873$  K  $< T < 2473$  K, and (d)  $T > 2473$  K. Reproduced with permission from Ref. 10.

X-ray diffraction data, indicating the nanographene units cannot be totally restored to the original structure by thermal treating at 3073 K.

Here we propose a simplified structure model for describing the porosity change and growth of graphitic structures during the high temperature treatment. The non-treated PGM is composed of randomly bridged nanographene sheets, which construct the interspaces known as micropores and mesopores, as shown in Figure 11(a). The structural model for non-treated PGM is similar to that provide in Figure 3 except the orientations of the graphitic units are given in a more randomly way, which is more close to the real situation. This structural model is also suitable for PGM samples treated below 1373 K. When sample is heat treated within the temperature regions of  $1373$  K  $< T < 1873$  K, the stacking of the nanographene layers start to occur, which consumes both micropores

and mesopores, as shown in Figure 11(b). The coalescence of nanographenes happens at the heating temperature above 1873 K, resulting in the formation of graphitic crystallites together with consumption of micropores and mesopores, as shown in Figure 11(c). The well-crystalline graphite structure form at the heating temperature above 2473 K and improve forward at higher temperatures. However, the nanoporosity almost all disappear under these temperatures, as shown in Figure 11(d).

The high temperature treatment brings about the opposite effect on crystallinity and porosity, which are both favored in various applications. It is not easy to solve this contradiction at this moment. However, it is still meaningful if certain degree of porosity can be traded to gain a higher electrical performance. For example, if the PGM is thermal treated at 1673 K, 18 % of its surface area will lost, but its electrical

conductivities are 36%, 52% and 200% higher than that of pristine PGM at temperature of 273 K, 77.4 K (liquid N<sub>2</sub>) and 4.2 K (liquid He), respectively. The increase of electrical performance at a small compensation of porosity should shed new light to the scientific perspective.

## 6. Ultralight graphene monoliths from shape-retention activation

Carbon monoliths with structural designability and hierarchical porosity have attracted significant attention in recent years. The monolith form of carbon has advantages over powdered forms such as high electrical and thermal conductivities, easy handling and so on (45-47), while the hierarchical porosity with micropore, mesopore and macropore can provide a combination of high surface area and efficient mass transportation, guaranteeing their good performance in the application of en-

grated graphene monolith with high surface area can be fabricated through an KOH activation process. However, a remarkable structural deformation of the monolith is observed, then a new KOH-activation route for a better structural designability is highly desired. In this review a modified KOH activation process is introduced, as shown in Figure 12. The RGO monolith was firstly prepared by the aforementioned method. The obtained RGO monolith was filled with KOH solution with the KOH to carbon weight ratio of 10/1, then quickly dipped into liquid N<sub>2</sub> to achieve a rapid freezing followed by freeze-drying for 24 h under vacuum condition (< 10 Pa). This is because the direct-heating of the RGO monolith filled with KOH solution leads to a serious deformation of its monolith shape. The obtained monolith loaded with KOH was activated at 973 K followed by washing with 0.1 M HCl aqueous solution and

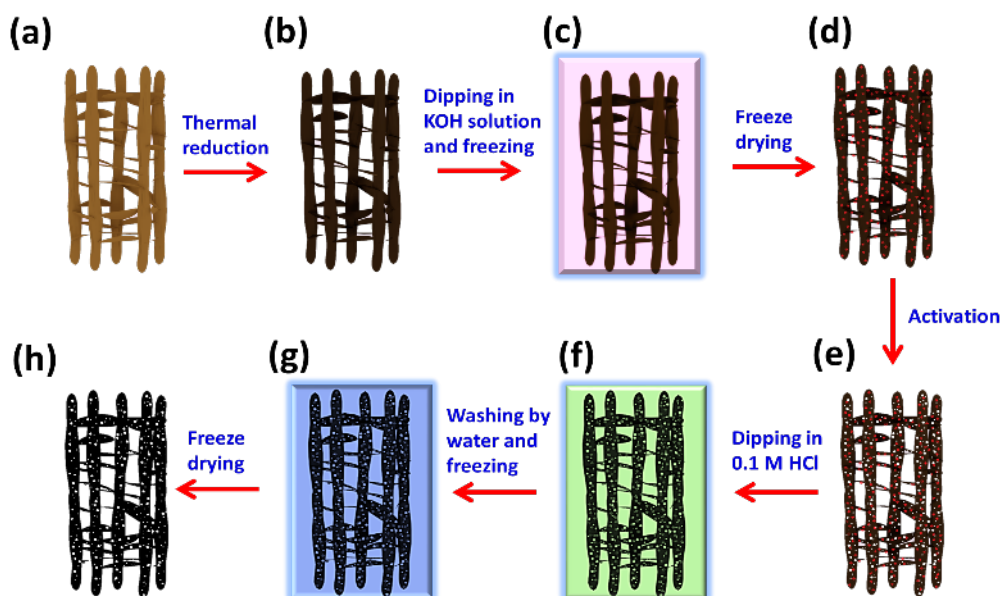


**Figure 12.** Schematic illustration of shape-retention activation process of graphene monoliths.

ergy and environmental (48-50). As mentioned in the previous chapter, the inte-

deionized water. Consequently, the products were rapidly frozen by liquid N<sub>2</sub> and

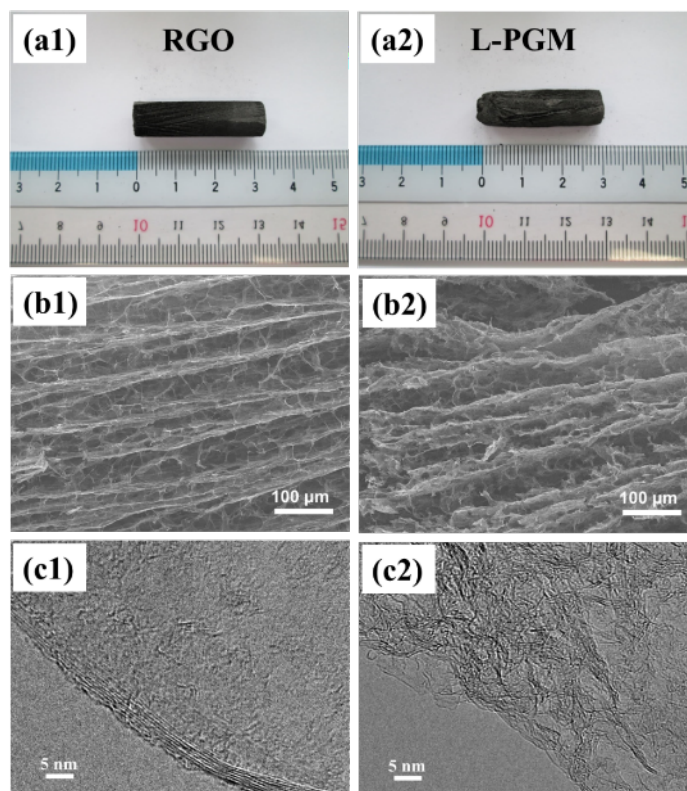


**Figure 13.** Morphology of RGO monolith before and after shape-retention activation. (a) Photos, (b) SEM images and (c) TEM images of RGO monolith and L-PGM. Reproduced with permission from Ref. 11.

freeze-dried again. The obtained porous graphene aerogel monoliths can maintain its original geometry with less than 10% shrinkage of volume, and the bulk density evaluated is  $8 \pm 0.5 \text{ mg cm}^{-3}$ , being extremely low. The ultralight porous graphene monolith is nominated as L-PGM in this review.

The photos of RGO monolith before and after shape-retention activation are shown in Figure 13(a). The RGO monolith has a cylindrical shape which is derived from the preparation mold, and the diameter and length of the monolith is about 1 and 3 cm, respectively. L-PGM prepared from the shape-retention activation can largely preserve the initial geometry of RGO monolith with less than 10% of volume shrinkage. The apparent density of L-PGM is about 8

$\pm 0.5 \text{ mg cm}^{-3}$ , being much lower than conventional activated carbons. The SEM images shown in Figure 13(b) clearly indicate the morphology change of RGO monolith before and after the KOH activation. The pristine RGO monolith have a unidirectional texture structure paralleling to the direction of ice growth, which is similar to the reported materials produced by ice-freezing method (16, 17). The well-aligned graphene sheets and inter-sheet bridging structure can be observed within the unidirectional texture structure. After KOH activation process the parallel unidirectional structures are still maintained, even if some parts of the graphene layers are slightly distorted and fractured. The well-preserved long-range parallel sheet structures guarantee the

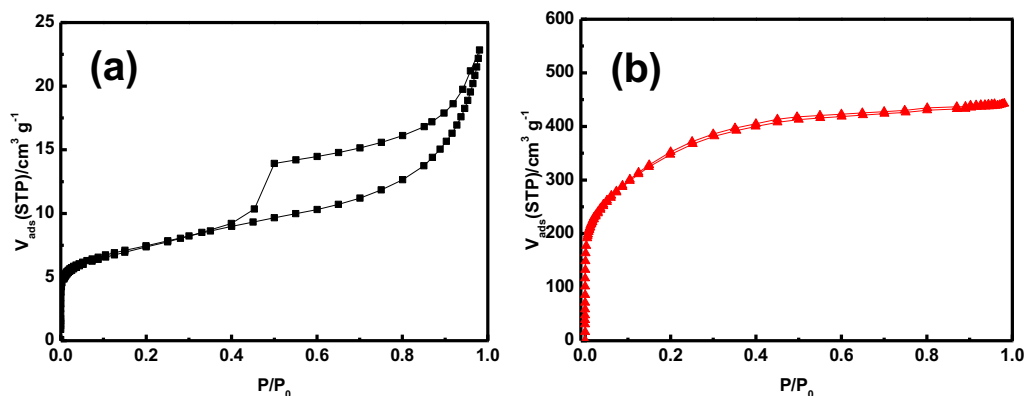


**Figure 14.**  $\text{N}_2$  adsorption-desorption isotherms of RGO monoliths before and after shape-retention activation. (a) RGO monolith. (b) L-PGM. Reproduced with permission from Ref. 11.

maintaining of free-standing nature. The TEM images shown in Figure 13(c) illustrate the microscopic structural change of RGO monolith before and after KOH activation. The pristine RGO monolith consists of uniformly stacked graphene layers with size more than several hundred nanometers. After the KOH activation process, the ordered stacking of graphene layers is degraded into entangled graphene sheets, giving nanoporous structure, as shown in Figure 13(c2). Even so, graphene sheets are much larger than the graphitic unit of conventional activated carbon, and their entangled and interconnected structure guarantees the firmness of the unidirectional texture structure in the free-standing monolith.

The porosity development of L-PGM through KOH activation is evaluated with the  $\text{N}_2$  adsorption isotherms at 77.4 K, as shown in Figure 14. The  $\text{N}_2$  adsorption-desorption of L-PGM is of type IV(a) with type H4 hysteresis loop, suggesting the presence of slit-shaped mesopores (19). After the shape-retention activation, the  $\text{N}_2$

adsorption-desorption of L-PGM changes to type I(b), indicating the development of micropores. The surface area of graphene monolith evaluated with SPE method increases from 26  $\text{m}^2 \text{g}^{-1}$  to 990  $\text{m}^2 \text{g}^{-1}$ . Thus-produced monolith has both abundant microporosity and macroporosity. Such unique hierarchical porous structure guarantees its wide application in the field that require both fast transportation and efficient adsorption.

## 7. Polymer enforced monoliths

The mechanical stability of a monolith is also essentially important for industrial applications. Even though the aforementioned monoliths are strong enough to provide a free-standing shape, their solidity is considerably weak. One route for producing strengthened monoliths is through soaking the RGO monoliths with a poly(ammonium-4-styrene sulfonate) water soluble polymer followed by carbonization at 1123 K (12). The obtained polymer enforced monoliths is nominated as P-RGO in this review.

The mechanical strength testaments for GO monolith, RGO monolith and the polymer enforced monoliths (P-RGO) monolith are shown in Figure 15. Remarkable deformation are observed on GO and RGO

P-RGO have quite homogenous pores with the pore width of 0.7 nm. the surface area evaluated by using SPE method is 345 m<sup>2</sup>/g.

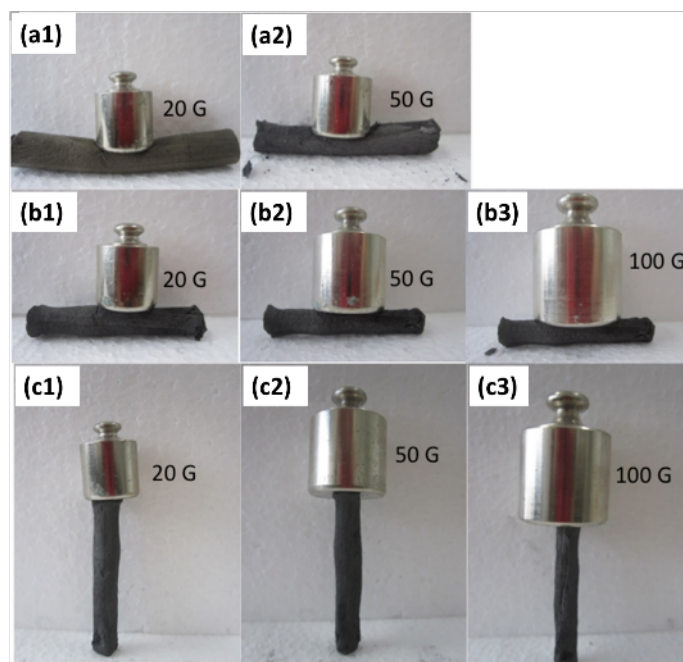


**Figure 15.** Comparison of the strength of the pristine and polymer enforced monoliths. The diameter of HT-MRP monolith is 7 mm. Reproduced with permission from Ref. 12.

monoliths when 20 g and 50 g weights are applied horizontally on them, respectively. On the other hand, P-RGO can maintain its original shape even when 100 g was applied in both vertical and horizontal directions, indicating its remarkable strength. The tolerable external pressure of P-RGO are estimated to be above 30 kPa.

The microscopic morphology study of P-RGO indicates that the graphene sheets of the monolith was uniformly covered by the polymer-derived carbon, which not only increase the contact between the graphene sheets, but also apparently increase the overall graphitization level according to the Raman spectroscopy. Porosity analysis with N<sub>2</sub> adsorption at 77.4 K showed that

### Conclusion

This paper describes the porosity control on porous graphene monoliths through the chemical reagent activation (KOH, ZnCl<sub>2</sub> and H<sub>3</sub>PO<sub>4</sub>), the CO<sub>2</sub> activation and the thermal treatment. Besides, the preparation of porous graphene monoliths of unidirectionally oriented texture and the monolith with good mechanical properties are also introduced. The KOH activation method is highly efficient for the production of high surface area graphene monolith, being promising for preparing pore width-tunable nanoporous carbons. On the other hand, activation with CO<sub>2</sub> and chemical reagent like ZnCl<sub>2</sub> and H<sub>3</sub>PO<sub>4</sub> show less effect on porosity development.

Thermal treatment of highly porous graphene monolith up to 3073 K can produce porous carbons with a wide surface area distribution from 1560 m<sup>2</sup>g<sup>-1</sup> to 10 m<sup>2</sup>g<sup>-1</sup>. The crystallinity study indicates that heat treatment brings about the growth of ordered graphitic structure on graphene-based porous carbon, being favorable for the recovering of unique physical properties of graphite. We also successfully prepared highly microporous graphene aerogel monolith of unidirectional texture structure through a shape-retention activation route, i.e., freeze-drying was employed in each drying step of the preparation process to protect the frameworks. Furthermore, a relatively rigid graphene based monoliths with ultramicropores uniformly developed in the monolith was prepared by using the polymer enhancing method. It is expected that with the effort of our work, researchers can get more insight for developing graphene-based porous carbons with novel structures and fascinating applications.

### Acknowledgement

Structural coordinates of the molecular model in the graphical abstract were supplied by C. de Tomas.

### Reference

- 1) H. B. Heersche, P. Jarillo-Herrero, J. B. Oostinga, L. M. K. Vandersypen, A. F. Morpurgo, *Nature*, **2006**, 446, 56–59.
- 2) Z. Qiao, J. Jung, Q. Niu, A. H. MacDonald. *Nano Lett.*, 2011, 11, 3453–3459.
- 3) P. Avouris, *Nano Lett.*, **2010**, 10, 4285–4294.
- 4) T. Kim, G. Jung, S. Yoo, K. S. Suh, R. S. Ruoff, *ACS Nano*, **2013**, 7, 6899–6905.
- 5) Y. Zhu, S. Murali, M. D. Stoller, K. J. Ganesh, W. Cai, P. J. Ferreira, et al, *Science*, **2011**, 332, 1537–1541.
- 6) G. M. Wang, H.Y. Wang, X. H. Lu, Y. C. Ling, et al, *Adv. Mater.*, **2013**, 25, 5336–5342.
- 7) H. Wang, Z. Xu, Z. Li, K. Cui, J. Ding, et al, *Nano Lett.*, **2014**, 14, 1987–1994.
- 8) M. A. Worsley, S. O. Kucheyev, H. E. Mason, M. D. Merrill, et al. *Chem. Commun.*, **2012**, 48, 8428–8430.
- 9) S. Wang, F. Tristan, D. Minami, T. Fujimori, R. Cruz-Silva, M. Terrones, K. Takeuchi, K. Teshima, F. Rodríguez -Reinoso, M. Endo, K. Kaneko, *Carbon*, **2014**, 76, 220–231.
- 10) S. Wang, A. Morelos-Gómez, Z. Lei, M. Terrones, K. Takeuchi, W. Sugimoto, M. Endo, K. Kaneko, *Carbon*, **2016**, 96, 174–183.
- 11) S. Wang, Z. Wang, R. Futamura, M. Endo, K. Kaneko, *Chem. Phys. Lett.*, **2017**, 673, 38–43.
- 12) T. J. Bandoz, S. Wang, D. Minami, K. Kaneko, *Carbon*, **2015**, 87, 87–97.
- 13) M. A. Lillo-Ródenas, D. Cazorla -Amorós, A. Linares-Solano, *Carbon*, **2003**, 41, 267–275.
- 14) H. Marsh, D. S. Yan, T. M. O'Grady, A. Wennerberg, *Carbon*, **1984**, 22, 603–611.
- 15) D. C. Marcano, D. V. Kosynkin, J. M. Berlin, A. Sinitskii, Z. Sun, A. Slesarev, et al, *ACS Nano*, **2010**, 4, 4806–4814.
- 16) S. R. Mukai, H. Nishihara, H. Tamon, *Chem. Commun.*, **2004**, 874–875.
- 17) N. Zhang, H. Qiu, Y. Si, W. Wang, J. Gao, *Carbon*, **2011**, 49, 827–837.
- 18) N. Setoyama, T. Suzuki, K. Kaneko, *Carbon*, **1998**, 36, 1459–1467.
- 19) K. S. W. Sing, D. H. Everett, R. A. W. Haul, L. Moscou, R. A. Pierotti, J. Rouquerol, T. Siemieniowska, *Pure & Appl Chem*, **1985**, 57, 603–619.
- 20) M Endo, T Furuta, F Minoura, C Kim, K Oshida, G Dresselhaus, M. S. Dresselhaus, *Supramolecular Sci.*, **1998**, 5, 261–266.

- 21) P. J. F. Harris, Z. Liu, K. Suenaga, J. Phys.: Condens. Matter., **2008**, 20, 362201–362205.
- 22) H. Wang, Q. Gao, J. Hu. J. Am. Chem. Soc., **2009**, 131, 7016–7022.
- 23) H. Marsh, D. A. Taylor, J. R. Lander, Carbon, **1981**, 19, 375–381.
- 24) M. Turmuzi, W. R. W. Daud, S. M. Tasirin, M. S. Takriff, S. E. Iyuke, Carbon, **2004**, 42, 453–455.
- 25) M. Molina-Sabio, M. T. Gonzalez, F. Rodríguez-Reinoso, A. Sepúlveda- Escribano, Carbon, **1996**, 34, 505–509.
- 26) H. Marsh, F. Rodríguez-Reinoso, Activated carbon, London: Elsevier. **2006**, P268, P330–P331.
- 27) M. Olivares-Marín, C. Fernández- González, A. Macías-García, V. Gómez- Serrano, Appl. Surf. Sci., **2006**, 252, 5967–5971.
- 28) S. Yorgun, N. Vural, H. Demiral, Micropor. Mesopor. Mat., **2009**, 122, 189–194.
- 29) H. Teng, T. S. Yeh, L. Y. Hsu, Carbon, **1998**, 36, 1387–1395.
- 30) F. Suárez-García, A. Martínez-Alonso, J. M. D. Tascón. Carbon, **2004**, 42, 1419–1426.
- 31) G.-B. Zheng, H. Sano, Y. Uchiyama, Carbon, **2003**, 41, 853–856.
- 32) M. B. Vázquez-Santos, E. Geissler, K. László, J.-N. Rouzaud, A. Martínez-Alonso, J. M. D. Tascón, J. Phys. Chem. C, **2012**, 116, 257–268.
- 33) T. Ohkubo, C.-M. Yang, E. Raymundo-Piñero, L. Solano, K. Kaneko, Chem. Phys. Lett., **2000**, 329, 71–75.
- 34) A. Bougrine, N. Dupont-Pavlovsky, A. Naji, J. Ghanbaja, J. F. Maréché, D. Billaud, Carbon, **2001**, 39, 685–695.
- 35) T. Shimada, T. Sugai, C. Fantini, M. Souza, L. G. Caçado, A. Jorio, et al, Carbon, **2005**, 43, 1049–1054.
- 36) M. S. Dresselhaus, A. Jorio, M. Hofmann, G. Dresselhaus, R. Saito, Nano Lett., **2010**, 10, 751–758.
- 37) L. M. Malard, M. A. Pimenta, G. Dresselhaus, M. S. Dresselhaus, Phys. Rep., **2009**, 473, 51–87.
- 38) F. Tuinstra, J. L. Koenig, J. Chem. Phys., 1970, 53, 1126–1130.
- 39) D. Mattia, M. P. Rossi, B. M. Kim, G. Korneva, H. H. Bau, Y. Gogotsi, J. Phys. Chem. B, **2006**, 110, 9850–9855.
- 40) M. J. Matthews, M. A. Pimenta, G. Dresselhaus, M. S. Dresselhaus, M. Endo, Phys. Rev. B, **1999**, 59, R6585–R6588.
- 41) Z. Q. Li, C. J. Lu, Z. P. Xia, Y. Zhou, Z. Luo, Carbon, **2007**, 45, 1686–1695.
- 42) H. Takagi, K. Maruyama, N. Yoshizawa, Y. Yamada, Y. Sato, Fuel, **2004**, 83, 2427–2433.
- 43) A. Oberlin, Carbon, **1984**, 22, 521–541.
- 44) F. G. Emmerich, Carbon, **1995**, 33, 1709–1715.
- 45) D. Menard, X. Py, N. Mazet, Chem. Eng. Process., **2007**, 46, 565–572.
- 46) A. M. Kern, B. Zierath, J. Haertlé, T. Fey, B. J. M. Etzold, Chem. Eng. Technol., **2016**, 39, 1121–1129.
- 47) Y. Li, J. Chen, L. Huang, C. Li, J.-D. Hong, G. Shi, Adv. Mater., **2014**, 26, 4789–4793.
- 48) Y. Li, Z. Li, P. K. Shen, Adv. Mater., **2013**, 25, 2474–2480.
- 49) C. Hoffmann, S. Thieme, J. Brückner, M. Oschatz, T. Biemelt, G. Mondin, H. Althues, S. Kaskel, ACS Nano, **2014**, 8, 12130–12140.
- 50) C. M. A. Parlett, K. Wilson, A. F. Lee, Chem. Soc. Rev., **2013**, 42, 3876–3893.